Article

Building wet planets through high-pressure magma–hydrogen reactions

https://doi.org/10.1038/s41586-025-09630-7

Received: 5 June 2023

Accepted: 15 September 2025

Published online: 29 October 2025

Open access

Check for updates

H. W. Horn[1,4]✉, A. Vazan[2], S. Chariton[3], V. B. Prakapenka[3] & S.-H. Shim[1]✉

Close-in transiting sub-Neptunes are abundant in our Galaxy[1]. Planetary interior models based on their observed radius–mass relationship suggest that sub-Neptunes contain a discernible amount of either hydrogen (dry planets) or water (wet planets) blanketing a core composed of rocks and metal[2]. Water-rich sub-Neptunes have been believed to form farther from the star and then migrate inwards to their present orbits[3]. Here we report experimental evidence of reactions between warm, dense hydrogen fluid and silicate melt that release silicon from the magma to form alloys and hydrides at high pressures. We found that oxygen liberated from the silicate melt reacts with hydrogen, producing an appreciable amount of water up to a few tens of weight per cent, which is much greater than previously predicted based on low-pressure ideal gas extrapolation[4,5]. Consequently, these reactions can generate a spectrum of water contents in hydrogen-rich planets, with the potential to reach water-rich compositions for some sub-Neptunes, implying an evolutionary relationship between hydrogen-rich and water-rich planets. Therefore, detection of a large amount of water in exoplanet atmospheres may not be the optimal evidence for planet migration in the protoplanetary disk, calling into question the assumed link between composition and planet formation location.

Water is an important building block of planets and a key ingredient of their potential habitability. The notion that water is incorporated into planetary bodies through condensation at sufficiently low temperatures in the outer protoplanetary disk seems to explain the architecture of the solar system well: the inner planets are mostly dry and rocky, sometimes with a small amount of water delivered from the outer solar system, whereas Uranus and Neptune—which are believed to be ice giants—exist outside the snow line[6]. However, some nebular hydrogen-rich gas was possibly captured and stored as H_2O in the deep interior of Earth after reacting with silicates[7–9].

NASA's Kepler mission has discovered many of close-in transiting exoplanets between Earth-like and Neptune-like in size (1–4 Earth radius, R_E) and density[10]. Planets with radii of 2–4R_E are typically modelled with rocky cores and envelopes dominated by either hydrogen or water, making their composition and formation ambiguous (where 'core' refers to the non-volatile interior, as commonly defined in exoplanet literature). A drop in relative frequency of occurrence among such planets was identified at 1.5–2R_E (that is, the radius valley)[1], which seems to divide planets into two groups: rocky + metallic Earth-like density with tiny or no atmosphere at 1–1.5R_E (that is, super-Earths), and rocky + metallic core with thick atmosphere at 2–4R_E (that is, sub-Neptunes). Models involving massive gas loss can explain the radius valley well[11,12], which seems to support hydrogen-dominated atmospheres, whereas other models explain the radius valley by two separate populations of dry and water-rich planets[13,14]. Moreover, some systems may host water-rich sub-Neptunes[15–17]. An important question for water-rich sub-Neptune models is how planets with a substantial water mass fraction can exist in close-in orbits if water mainly condensed and was incorporated into planets in the outer part of the systems during their formation[3].

In classical models of sub-Neptunes with hydrogen-rich envelopes, hydrogen is typically assumed not to react with silicates and metals in the core, although physical mixing with silicate magma has been considered[18,19]. At low pressures and high temperatures, hydrogen can reduce cations in silicates and oxides to metals[20], releasing oxygen from melts and producing water through hydrogen oxidation. Experimental data show that hydrogen can reduce Fe^{2+} to Fe^0 in molten silicates, generating water at low pressure[7,21,22], and this trend extends to higher pressures[23]. However, in protoplanetary disks, most iron is metallic, with only limited Fe^{2+} and Fe^{3+} available. Recent experiments show that Mg remains oxidized in dense hydrogen, but small amounts of MgH_2 can form, releasing oxygen for water production[24]. Thermodynamic models based on low-pressure data suggest that hydrogen cannot reduce a substantial amount of Si^{4+} in silicates to produce water[5,7]. A modelling study indicates that enhanced Si partitioning into metal under reducing conditions could yield Earth-like water abundances (about 10^{-2} wt%) (ref. 9). However, experiments show that SiO_2 can dissolve in hydrogen at 2–15 GPa and 1,400–1,700 K, with Si–O bonds breaking to form Si–H, suggesting that pressure may promote hydrogen–silicate reactions[25,26].

If the mass–radius of sub-Neptunes is modelled with a rock + metal core with a hydrogen-dominated envelope, the pressure at the

[1]School of Earth and Space Exploration, Arizona State University, Tempe, AZ, USA. [2]Astrophysics Research Center, Department of Natural Sciences, Open University of Israel, Ra'anana, Israel. [3]Center for Advanced Radiation Sources, The University of Chicago, Chicago, IL, USA. [4]Present address: Lawrence Livermore National Laboratory, Livermore, CA, USA. ✉e-mail: hallensu@asu.edu; sshim5@asu.edu

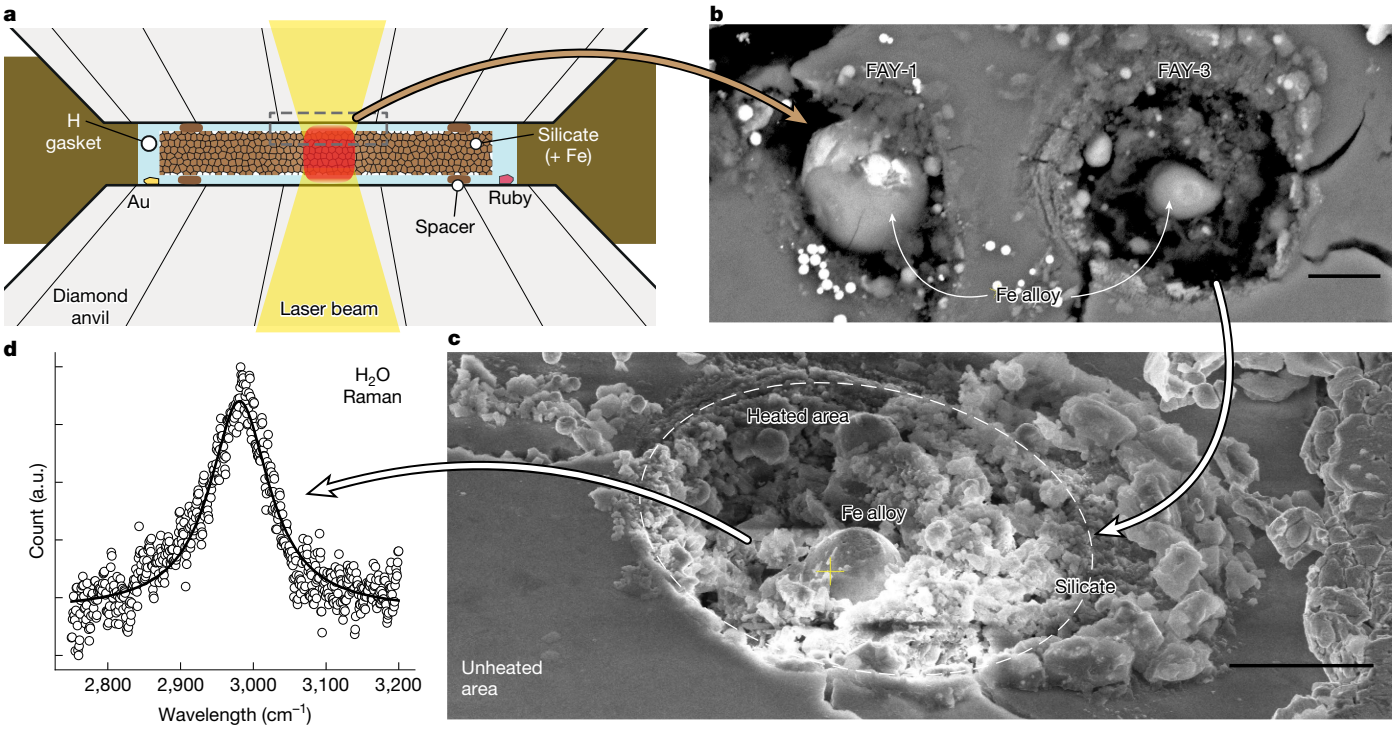

Fig. 1 | Laser-heated diamond-anvil cell experiments on silicate melts in a hydrogen medium. a, Schematic of the experimental setup. The spacers (small single grains of the same material from which the foil was made) separate the sample foil from diamond anvils, which allow hydrogen to surround the sample. During laser heating (the red area at the centre) of the silicate sample, hydrogen penetrated the grain boundaries of the sample foil and immediately above and below were heated by thermal conduction. **b**, An SEM image of two laser-heated areas of a fayalite sample. FAY-1 was heated at 6 GPa and 3,017 K and FAY-3 was heated at 11 GPa and 2,898 K. The spheres at the centre of the heated areas are Fe-rich alloys formed by hydrogen–silicate reaction. **c**, An SEM image of FAY-3 from an angle for a wider area. **d**, Raman-active OH vibration from H_2O ice after heating silica + Fe metal in a hydrogen medium at 14 GPa. A full two-dimensional Raman map of the heated area is shown in Extended Data Fig. 3c. Scale bars, 5 μm (**b**,**c**).

core-envelope boundary (CEB) can exceed a few GPa (ref. 27). This blanketing envelope can also decrease heat loss such that silicates and metals of the core remain molten for billions of years (ref. 28). Under these conditions, hydrogen is a dense fluid. Therefore, it is essential to understand the behaviour of the hydrogen–silicate system at the high pressures and temperatures (P–T) that exist at such a CEB. However, to our knowledge, these data do not exist. In this study, we combined pulsed laser heating[29] with the diamond-anvil cell to mitigate diamond embrittlement, which has been the main problem in melting silicate and metal in a pure hydrogen medium to acquire key data for understanding possible hydrogen–silicate reactions at the P–T conditions expected at the CEB in sub-Neptunes (Fig. 1, Extended Data Figs. 1 and 2, Extended Data Table 1 and Supplementary Discussion 1).

High-pressure magma–hydrogen reactions

A starting mixture of San Carlos olivine, $(Mg_{0.9}Fe_{0.1})_2SiO_4$, and iron metal was melted in a hydrogen medium at 8 GPa (Extended Data Table 1, run SCO-3). After heating, high-pressure X-ray diffraction (XRD) patterns showed no peaks from silicates, including olivine (Fig. 2a). Instead, diffraction lines of B2 $Fe_{1-y}Si_y$ were observed, showing that Si^{4+} in silicate melt was reduced to Si^0 and alloyed with Fe metal. After heating, Mg remains in MgO periclase. The unit-cell volume of MgO after decompression to 1 bar indicates no detectable Fe^{2+} in the phase. Therefore, all Fe^{2+} originally in the silicate is also reduced to Fe^0 metal, implying the following reaction:

$$(Mg_{0.9}Fe_{0.1})_2SiO_4 + 0.8Fe + 2.2H_2 \rightarrow FeSi + 1.8MgO + 2.2H_2O. \quad (1)$$

In our experiments, 20 wt% of Fe metal was mixed with olivine and a smaller amount of Fe metal was formed from the reduction of Fe^{2+} in olivine. If all the Fe metal is consumed to form FeSi (that is, $y = 0.5$ in $Fe_{1-y}Si_y$), a maximum of 86% of the Si^{4+} in olivine can be reduced (Supplementary Code 1). However, the measured unit-cell volume of the Fe–Si alloy indicates $y = 0.27$ in $Fe_{1-y}Si_y$ (Supplementary Discussion 2–8). Therefore, only 32% of Si^{4+} in olivine was reduced to form an alloy with Fe metal. Furthermore, FeH_x alloys in the face-centred cubic (fcc) and double hexagonal close-packed (dhcp) structures ($x = 0.22$–0.4) were found after heating, thus decreasing the amount of Fe metal available to form Fe–Si alloys. The observation of the complete disappearance of silicates after melting in dense hydrogen fluid requires an additional process to remove Si^{4+} from silicates.

Previous experiments at similar pressures but lower temperatures[25,26] showed the release of Si^{4+} from silicate and dissolution in dense fluid hydrogen as SiH_4:

$$Mg_2SiO_4 + 4H_2 \rightarrow SiH_4 + 2MgO + 2H_2O. \quad (2)$$

We detected the same Si–H bond vibration in melted areas in our experiment (Extended Data Fig. 4 and Supplementary Discussion 9). Both the reduction and hydride formation reactions (reactions 1 and 2, respectively) involve the release of O, which can then react with H to form H_2O. The OH vibration from H_2O was unambiguously detected in melted areas with Raman spectroscopy (Fig. 1d and Extended Data Fig. 3). The same behaviour was also observed at pressures up to 22 GPa in multiple experimental runs (Extended Data Fig. 5 and Supplementary Discussion 2 and 3).

When olivine + Fe was heated at 42 GPa to temperatures below the melting temperature[30], olivine transformed to bridgmanite (bdm) and

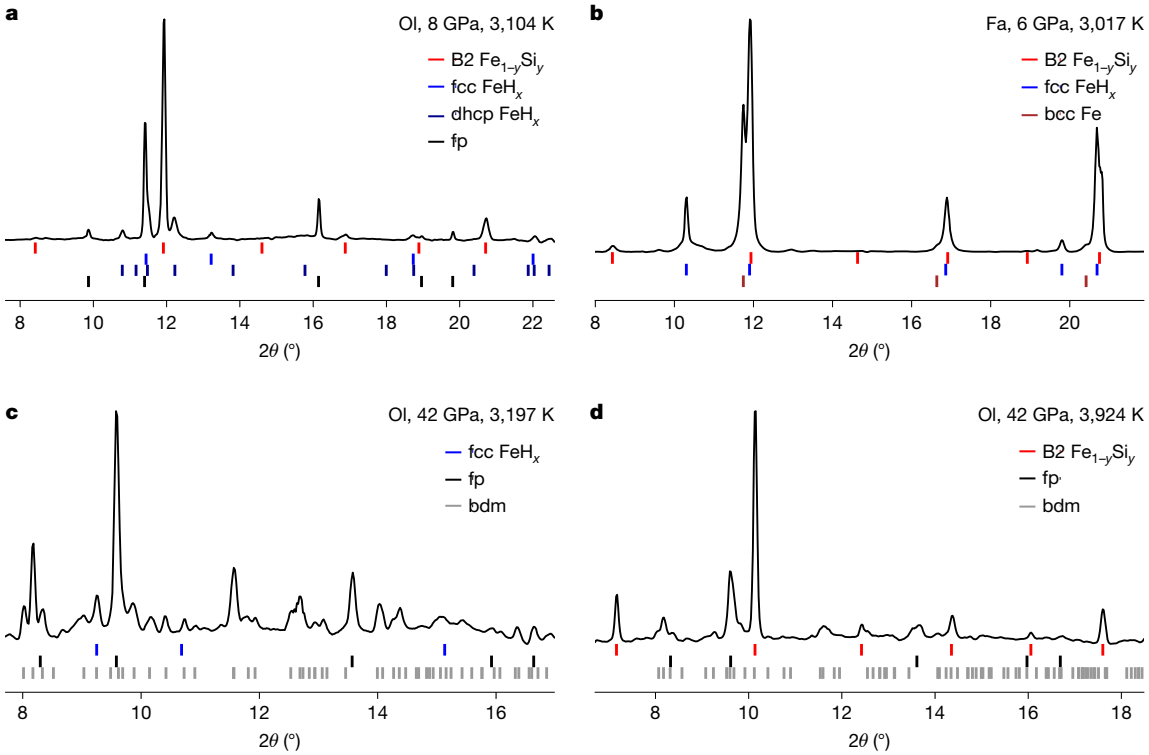

Fig. 2 | XRD patterns after heating silicate samples in a hydrogen medium. **a**, In run SCO-3, olivine breaks down to Fe metal alloys and MgO. **b**, In run FAY-1, fayalite breaks down with Fe and Si present as metal alloys. A very small amount of body-centred cubic (bcc) Fe may exist. **c**, Heating to temperatures below melting (2,725–3,197 K), bridgmanite (bdm) and ferropericlase (fp) appear at 42 GPa (SCO-13a). **d**, When the bdm + fp were melted (3,352–3,924 K at 42 GPa), bdm mostly breaks down and B2 $Fe_{1-y}Si_y$ appears (run SCO-13b). X-ray energy is 30 keV for **b** and 37 keV for **a**, **c** and **d**. The ticks below the diffraction patterns are the peak positions of the observed phases. fcc, face-centred cubic; dhcp, double hexagonal close-packed; Ol, San Carlos olivine starting material; Fa, fayalite starting material.

ferropericlase (fp) (Fig. 2c). We further heated the synthesized bdm + fp above the melting temperature of bdm. Most of the bdm dissociates on melting in a hydrogen medium (Fig. 2d). The SiO_2 component reacts with H and Fe to form B2 $Fe_{1-y}Si_y$ (Extended Data Fig. 3a,b). The volume measured for quenched fp suggests the complete reduction of Fe^{2+} to Fe^0 (Supplementary Discussion 4).

With fayalite (Fe_2SiO_4) and SiO_2 + Fe metal, we observed consistent behaviours, including formation of H_2O (Fig. 1d), SiH_4 (Extended Data Fig. 4), B2 $Fe_{1-y}Si_y$ (Extended Data Fig. 6) and FeH_x (Fig. 2b) (Extended Data Figs. 7–9; Supplementary Discussion 5). SiH_4 was detected in runs in which fayalite was melted in an Ar medium with 50% H_2 (Supplementary Discussion 9). In this case, the relative content of H_2O (formed from the reaction) compared with H_2 is much higher because of the decreased initial concentration of H and the increased H_2O production from the Fe^{2+} in the silicate, resulting in far more oxidizing conditions. In SiH_4, Si remains oxidized and, therefore, water production can continue as the water concentration rises through the formation of SiH_4 rather than Fe–Si metal (equation (2)).

Implications of reaction for planets

In a sub-Neptune planet with a rocky core and a substantial amount of hydrogen, the CEB is the most likely region to experience reactions between dense fluid hydrogen and silicate melt. The hydrogen–magma boundaries of these planets in the mass range of 3–10M_E (where M_E is mass of the Earth) with 2–20 wt% of H + He atmosphere are expected to reach P–T conditions similar to our experimental conditions for water production (Supplementary Discussion 10). According to our calculation in ref. [28], for a 5M_E rocky planet with a 5 wt% H_2 envelope, the temperature of the core remains sufficiently high to maintain the molten state of silicates for billions of years (Extended Data Fig. 2), which could, in turn, make the continuation of the observed reactions possible for billions of years. Moreover, because pressure greatly enhances H_2 solubility in magma[18] and can result in miscibility between hydrogen fluid and oxide melts[24], hydrogen can reach greater depths below the CEB. Vigorous convection in the molten core could also transport hydrogen further to greater depths. For all of these reasons, the reactions discussed can continue into the deep interior.

We combined equations (1) and (2) with constraints from experimental setups and observations to estimate the quantities of reactants and reaction products for olivine reacting with hydrogen in our experiments (Supplementary Discussion 11). Considering uncertainties (Supplementary Code 1), we calculated that before reacting, the sample volume that would be heated consisted of 4.5–5.7 wt% H_2, about 76 wt% silicate and about 19 wt% Fe metal. It shows that 18.1(5) wt% H_2O was produced. This composition lies within the range considered for sub-Neptunes[2]. The complete disappearance of silicate (and therefore release of all of the Si) at lower pressures suggests silicate-undersaturated conditions for the hydrogen-to-silicate mass ratio of our olivine + Fe metal experiment, which was estimated to be 0.06–0.08. For a sub-Neptune with 4 wt% H_2 and an Earth-like core composition, the hydrogen-to-silicate mass ratio is 0.06. Therefore, sub-Neptunes with a few wt% H_2 could provide a silicate-undersaturated condition with respect to hydrogen. At >25 GPa, a trace amount of bdm (silicate) remained in the reacted area (Fig. 2d), which could result from the reverse reaction and, therefore, suggest a possible equilibrium. If this is the case, even under equilibrium conditions, the amount of Si in the silicate melt consumed by the reaction is very large, and the H_2O produced can amount to tens of weight per cent (Supplementary Code 1).

A theoretical study considering the formation of SiH_4 at hydrogen–magma boundaries[4] predicted $X(H_2O) \approx 0.2$ (where X is a mole fraction

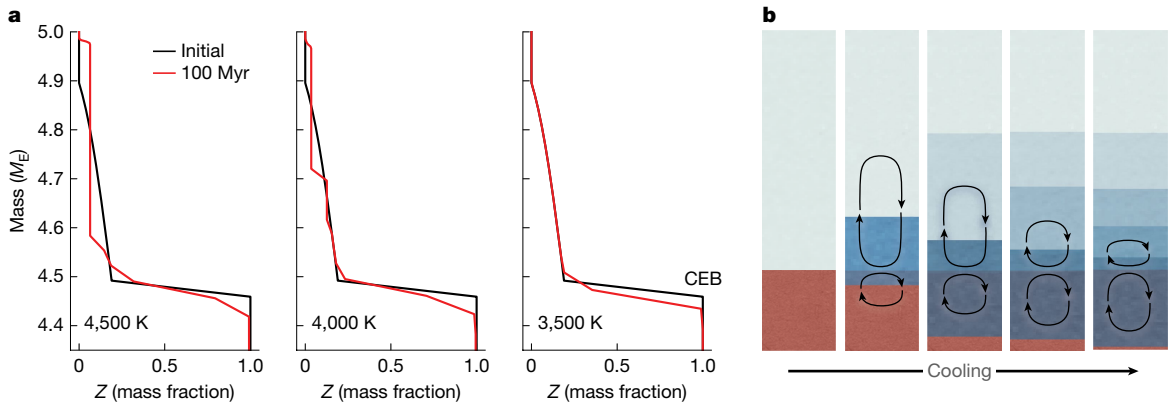

Fig. 3 | Water redistribution in a $5M_E$ planet with 10 wt% envelope made of H_2 and He. a, Water mass fraction (Z) for an initial state distribution (black) and after 100 Myr of evolution (red). Mixing efficiency decreases as the planet cools (left to right). **b**, The schematic shows the time progression of the mixing scale near the reaction zone.

in the envelope) of water production along with $X(SiH_4) \approx 0.04$, and $X(SiO) \approx 0.08$ in a $4M_E$ sub-Neptune with 2.5 wt% H_2 at about 10 GPa and 5,000 K. Another theoretical study[5] considering the reduction of Si predicted $X(H_2O) \approx 10^{-4}$–10^{-3} of water production for a $4M_E$ sub-Neptune with a CEB temperature of 4,500 K. At similar P–T conditions, however, our experimental observations indicate much more efficient endogenic water production of $X(H_2O) = 0.38$–0.56, which is 2–3,000 times higher. Although the modelling studies used extrapolation of assumed ideal gas behaviour of H_2 at much lower pressure, our experiments were conducted at the P–T conditions for dense fluid hydrogen, directly relevant to the conditions and states expected at the CEBs of sub-Neptunes. A comparison of our results with refs. 4,5 highlights the notable pressure effects on water production.

At a planetary scale, the extent of endogenic water production can be affected by the activity of H_2 and H_2O in the system. Under a hydrogen-dominated envelope lacking H_2O, strongly reducing conditions promote the reduction of Si as a key pathway for endogenic water production. As more water is produced (and therefore the activity of H_2 decreases), the reaction zone becomes less reducing. As the reaction progresses, if the water concentration reaches a point at which the conditions become sufficiently oxidizing, the reduction of Si could stop. In this case, SiH_4 would become a dominant Si-bearing product of the hydrogen–magma reaction because it does not require the reduction of Si^{4+}. Because of this, SiH_4 formation can occur at more oxidizing conditions than Fe–Si alloys, as shown in our experiments (Supplementary Discussion 9), prolonging endogenic water production to more oxidizing conditions.

The redox state of the reaction zone can also be affected by the dynamics of the region. In the absence of mixing and transport, the fraction of water near the reaction zone will increase, which will slow down and ultimately stop the water-producing reaction when the water concentration exceeds a critical value (which is not well constrained, but we estimate to be $X(H_2O) \geq 38$–56 mol%; Supplementary Discussion 11 and Supplementary Code 1). However, the interiors of sub-Neptunes by and large are convective, and therefore efficient mixing and transport can reduce the concentration of H_2O in the reaction zone. In Fig. 3a,b, we show an example of the efficiency of water-mixing over 100 million years in a $5M_E$ rocky planet with a 10% gas (H, He) envelope. For CEB temperatures of ≥4,500 K, water is almost completely mixed through convection in the envelope. The mixing efficiency decreases as the planet cools. Because water production continues up to $X(H_2O) > 0.3$, we anticipate that convective mixing may stop before water production has ended. Consequently, the deep envelope might be more water-rich than the outer envelope in these planets at CEB temperatures lower than about 3,500 K.

Hydrides also form in the reactions discussed here and in other experiments[24–26]. Only a small amount of MgH_2 was reported to be produced, and its formation is limited to temperatures much higher than 3,000 K (Supplementary Discussion 13). Estimates from our experiments (Supplementary Discussion 11) show 6–23(5) mol% SiH_4 can be produced, and, therefore, it is important to consider. Although no data exist directly at the P–T conditions of our study, existing data indicate that the density of SiH_4 is 20–30% lower than that of H_2O at 300 K and relevant pressures (Supplementary Discussion 14). Therefore, the upward transport of H_2O and SiH_4 away from the reaction zone could be more efficient than predicted by our model.

It is essential to note that at the P–T conditions we consider here, H_2 and H_2O are completely miscible and form a single fluid[31], whereas our dynamic model includes only convective mixing of two separate fluids of H_2 and H_2O. Similar to H_2O and H_2, existing data also support the miscibility between SiH_4 and H_2 at the conditions of the CEB. The miscibility will decrease the density of the fluid compared with pure H_2O, and the hydrogen contained in the dense fluid layer will still react with the magma ocean (Supplementary Discussion 14).

The increasing solubility of water in silicates at higher pressures (that is, ingassing)[32,33] can reduce its activity at the CEB and thus prolong the hydrogen–silicate reactions. Furthermore, the dissolved water decreases both the melting temperature and viscosity of the magma, prolonging the molten state of the interior and promoting efficient convective mixing of materials to the deeper undersaturated depths of the core. Therefore, strong ingassing of water (and hydrogen) to the core can also enable more water production.

The amount of endogenic water produced can vary depending on the properties and configurations of different planets (Supplementary Discussion 12). The Mg:Si ratio can directly affect the amount of water produced, as Si-involved reactions with hydrogen probably dominate endogenic water production compared with Mg and Fe (Supplementary Discussion 13). For example, for a planet with an Earth-like metal-to-silicate mass ratio but the Mg:Si ratio reduced from 2 to 0.5 (more Si), if all the silicate reacts with hydrogen (>3 wt% of H_2), the amount of water produced will increase from 16 wt% to 29 wt% (Supplementary Code 3). The Mg:Si ratio will also affect the viscosity of the magma and, therefore, affect the ingassing and mixing of volatile species[34]. Therefore, the large variation in Mg:Si ratios observed in exoplanetary systems[35] will result in variation in endogenic water production among planets with rocky interiors and hydrogen-dominated atmospheres.

The proposed atmospheric loss of the hydrogen-rich envelope of a sub-Neptune[11,12] may occur concurrently with the endogenic production of water. The timing and duration of these two processes are

important factors in the amount of water produced. Atmospheric loss also plays a part in the rate of heat loss, which, in turn, influences the duration for which the water-producing reactions can persist because they predominantly occur in molten silicates and metal alloys.

If a sub-Neptune undergoes massive gas loss while water is retained because of its high mean molecular mass[22,36], it is feasible that the limited water production that occurred concurrently with gas loss would result in a rocky planet with surface water. For example, for a $5M_E$ sub-Neptune, if only the outer 5% of the rocky core reacts with hydrogen, 2–4 wt% H_2O would be produced (Supplementary Code 2). At the same time, large amounts of water can also be stored in the core of sub-Neptunes because pressure increases the solubility of water in magma[32,33]. Therefore, even if surface or atmospheric water is lost during gas loss, the water stored in the core can contribute substantially to the formation of a secondary atmosphere and hydrosphere when the interior cools and solidifies, in which the solubility of water is much lower[22,37,38]. Moreover, because higher pressures markedly enhance water-producing reactions, super-Earths converted from hydrogen-rich sub-Neptunes may contain much more water than smaller rocky planets such as Earth.

Another key implication is that hydrogen-rich and water-rich sub-Neptunes do not necessarily form through different processes[39,40]. Instead, the reaction we report here suggests that these planet types may be fundamentally related: hydrogen-rich sub-Neptunes could be the precursors of water-rich sub-Neptunes and super-Earths. If an excess, unreacted H_2 atmosphere can be retained, sub-Neptunes with an H_2-rich atmosphere covering an H_2O-rich layer above the core (that is, hycean worlds) may be quite common[41].

In conventional planet-formation theory, water-rich planets are believed to form outside the snow line. The observation of water-rich sub-Neptunes[15–17,42,43] in close orbits raises important questions about how they can form. Models have been proposed to explain close-in transiting water-rich sub-Neptunes, such as migration of water worlds after their formation outside the snowline[3,40,44]. Endogenic water production through hydrogen–magma reactions observed in our experiments provides a straightforward process to build water-rich sub-Neptunes inside the snow line: close-in orbiting sub-Neptunes can be H_2O-rich planets, as the hydrogen–silicate reaction can convert the H-dominated atmosphere to H_2O from the inside out, almost independent of their radial distance from the stars. Water production is feasible and expected in the large population of $3–10M_E$ planets that were formed with substantial (>2%) gas envelopes. On planets with a hotter CEB, vigorous convection and sustained water production are expected to persist longer over their thermal evolution. Moreover, if mixing of water into the core is efficient, the production of water can persist even when convection in the water-polluted envelope becomes less efficient. This result has fundamental implications for planet formation and evolution theories. Based on experimental results, we suggest that planets formed from dry materials can become water-rich (tens of wt% water) planets without direct accretion of water ice. Consequently, detection of a large amount of water in exoplanet atmospheres might not be the optimal evidence for planet migration in the protoplanetary disk. Our new experimental findings challenge the assumed link between planet formation location and composition.

Online content

Any methods, additional references, Nature Portfolio reporting summaries, source data, extended data, supplementary information, acknowledgements, peer review information; details of author contributions and competing interests; and statements of data and code availability are available at https://doi.org/10.1038/s41586-025-09630-7.

1. Fulton, B. J. et al. The California-*Kepler* survey. III. A gap in the radius distribution of small planets. *Astron. J.* **154**, 109 (2017).
2. Bean, J. L., Raymond, S. N. & Owen, J. E. The nature and origins of sub-Neptune size planets. *J. Geophys. Res. Planets* **126**, e2020JE006639 (2021).
3. Bitsch, B. et al. Dry or water world? How the water contents of inner sub-Neptunes constrain giant planet formation and the location of the water ice line. *Astron. Astrophys.* **649**, L5 (2021).
4. Misener, W., Schlichting, H. E. & Young, E. D. Atmospheres as windows into sub-Neptune interiors: coupled chemistry and structure of hydrogen–silane–water envelopes. *Mon. Not. R. Astron. Soc.* **524**, 981–992 (2023).
5. Schlichting, H. E. & Young, E. D. Chemical equilibrium between cores, mantles, and atmospheres of super-Earths and sub-Neptunes and implications for their compositions, interiors, and evolution. *Planet. Sci. J.* **3**, 127 (2022).
6. Morbidelli, A. et al. Source regions and timescales for the delivery of water to the Earth. *Meteorit. Planet. Sci.* **35**, 1309–1320 (2000).
7. Ikoma, M. & Genda, H. Constraints on the mass of a habitable planet with water of nebular origin. *Astrophys. J.* **648**, 696 (2006).
8. Hallis, L. J. et al. Evidence for primordial water in Earth's deep mantle. *Science* **350**, 795–797 (2015).
9. Young, E. D., Shahar, A. & Schlichting, H. E. Earth shaped by primordial H_2 atmospheres. *Nature* **616**, 306–311 (2023).
10. Howard, A. W. et al. Planet occurrence within 0.25 AU of solar-type stars from *Kepler*. *Astrophys. J. Suppl. Ser.* **201**, 15 (2012).
11. Owen, J. E. & Wu, Y. *Kepler* planets: a tale of evaporation. *Astrophys. J.* **775**, 105 (2013).
12. Ginzburg, S., Schlichting, H. E. & Sari, R. Core-powered mass-loss and the radius distribution of small exoplanets. *Mon. Not. R. Astron. Soc.* **476**, 759–765 (2018).
13. Zeng, L. et al. Growth model interpretation of planet size distribution. *Proc. Natl Acad. Sci. USA* **116**, 9723–9728 (2019).
14. Venturini, J. & Helled, R. Jupiter's heavy-element enrichment expected from formation models. *Astron. Astrophys.* **634**, A31 (2020).
15. Luque, R. & Pallé, E. Density, not radius, separates rocky and water-rich small planets orbiting M dwarf stars. *Science* **377**, 1211–1214 (2022).
16. Piaulet, C. et al. Evidence for the volatile-rich composition of a 1.5-Earth-radius planet. *Nat. Astron.* **7**, 206–222 (2022).
17. Piaulet-Ghorayeb, C. et al. JWST/NIRISS reveals the water-rich "Steam World" atmosphere of GJ 9827 d. *Astrophys. J. Lett.* **974**, L10 (2024).
18. Hirschmann, M. M., Withers, A. C., Ardia, P. & Foley, N. T. Solubility of molecular hydrogen in silicate melts and consequences for volatile evolution of terrestrial planets. *Earth Planet. Sci. Lett.* **345**, 38–48 (2012).
19. Kite, E. S., Fegley, B. Jr, Schaefer, L. & Ford, E. B. Superabundance of exoplanet sub-neptunes explained by fugacity crisis. *Astrophys. J. Lett.* **887**, L33 (2019).
20. Sabat, K. C., Rajput, P., Paramguru, R. K., Bhoi, B. & Mishra, B. K. Reduction of oxide minerals by hydrogen plasma: an overview. *Plasma Chem. Plasma Process.* **34**, 1–23 (2014).
21. Kimura, T. & Ikoma, M. Predicted diversity in water content of terrestrial exoplanets orbiting M dwarfs. *Nat. Astron.* **6**, 1296–1307 (2022).
22. Krissansen-Totton, J., Wogan, N., Thompson, M. & Fortney, J. J. The erosion of large primary atmospheres typically leaves behind substantial secondary atmospheres on temperate rocky planets. *Nat. Commun.* **15**, 8374 (2024).
23. Horn, H. W., Prakapenka, V., Chariton, S., Speziale, S. & Shim, S.-H. Reaction between hydrogen and ferrous/ferric oxides at high pressures and high temperatures—implications for sub-neptunes and super-earths. *Planet. Sci. J.* **4**, 30 (2023).
24. Kim, T. et al. Stability of hydrides in sub-Neptune exoplanets with thick hydrogen-rich atmospheres. *Proc. Natl Acad. Sci. USA* **120**, e2309786120 (2023).
25. Shinozaki, A. et al. Influence of H_2 fluid on the stability and dissolution of Mg_2SiO_4 forsterite under high pressure and high temperature. *Am. Mineral.* **98**, 1604–1609 (2013).
26. Shinozaki, A. et al. Formation of SiH_4 and H_2O by the dissolution of quartz in H_2 fluid under high pressure and temperature. *Am. Mineral.* **99**, 1265–1269 (2014).
27. Stökl, A., Dorfi, E. A., Johnstone, C. P. & Lammer, H. Dynamical accretion of primordial atmospheres around planets with masses between 0.1 and 5 $M_\oplus$ in the habitable zone. *Astrophys. J.* **825**, 86 (2016).
28. Vazan, A., Ormel, C. W., Noack, L. & Dominik, C. Contribution of the core to the thermal evolution of sub-Neptunes. *Astrophys. J.* **869**, 163 (2018).
29. Goncharov, A. F. et al. X-ray diffraction in the pulsed laser heated diamond anvil cell. *Rev. Sci. Instrum.* **81**, 113902 (2010).
30. Shen, G. & Lazor, P. Measurement of melting temperatures of some minerals under lower mantle pressures. *J. Geophys. Res. Solid Earth* **100**, 17699–17713 (1995).
31. Gupta, A., Stixrude, L. & Schlichting, H. E. The miscibility of hydrogen and water in planetary atmospheres and interiors. *Astrophys. J. Lett.* **982**, L35 (2025).
32. Kim, T. et al. Atomic-scale mixing between MgO and H_2O in the deep interiors of water-rich planets. *Nat. Astron.* **5**, 815–821 (2021).
33. Hirschmann, M. M., Aubaud, C. & Withers, A. C. Storage capacity of H_2O in nominally anhydrous minerals in the upper mantle. *Earth Planet. Sci. Lett.* **236**, 167–181 (2005).
34. Karki, B. B., Ghosh, D. B. & Bajgain, S. K. in *Magmas Under Pressure* 419–453 (Elsevier, 2018).
35. Putirka, K. D. & Xu, S. Polluted white dwarfs reveal exotic mantle rock types on exoplanets in our solar neighborhood. *Nat. Commun.* **12**, 6168 (2021).
36. Aguichine, A., Mousis, O., Deleuil, M. & Marcq, E. Mass–radius relationships for irradiated ocean planets. *Astrophys. J.* **914**, 84 (2021).
37. Vazan, A., Sari, R. & Kessel, R. A new perspective on the interiors of ice-rich planets: ice-rock mixture instead of ice on top of rock. *Astrophys. J.* **926**, 150 (2022).
38. Luo, H., Dorn, C. & Deng, J. The interior as the dominant water reservoir in super-Earths and sub-Neptunes. *Nat. Astron.* **8**, 1399–1407 (2024).
39. Venturini, J., Guilera, O. M., Haldemann, J., Ronco, M. P. & Mordasini, C. The nature of the radius valley: hints from formation and evolution models. *Astron. Astrophys.* **643**, L1 (2020).
40. Burn, R. et al. A radius valley between migrated steam worlds and evaporated rocky cores. *Nat. Astron.* **8**, 463–471 (2024).

41. Madhusudhan, N., Piette, A. A. A. & Constantinou, S. Habitability and biosignatures of hycean worlds. *Astrophys. J.* **918**, 1 (2021).
42. Cherubim, C. et al. TOI-1695 b: a water world orbiting an early-M dwarf in the planet radius valley. *Astron. J.* **165**, 167 (2023).
43. Osborne, H. L. M. et al. TOI-544 b: a potential water-world inside the radius valley in a two-planet system. *Mon. Not. R. Astron. Soc.* **527**, 11138–11157 (2023).
44. Izidoro, A. et al. The exoplanet radius valley from gas-driven planet migration and breaking of resonant chains. *Astrophys. J. Lett.* **939**, L19 (2022).

Publisher's note Springer Nature remains neutral with regard to jurisdictional claims in published maps and institutional affiliations.

Open Access This article is licensed under a Creative Commons Attribution 4.0 International License, which permits use, sharing, adaptation, distribution and reproduction in any medium or format, as long as you give appropriate credit to the original author(s) and the source, provide a link to the Creative Commons licence, and indicate if changes were made. The images or other third party material in this article are included in the article's Creative Commons licence, unless indicated otherwise in a credit line to the material. If material is not included in the article's Creative Commons licence and your intended use is not permitted by statutory regulation or exceeds the permitted use, you will need to obtain permission directly from the copyright holder. To view a copy of this licence, visit http://creativecommons.org/licenses/by/4.0/.

© The Author(s) 2025

Methods

Sample materials and preparation

We studied three starting materials: (1) San Carlos olivine, $(Mg_{0.9}Fe_{0.1})_2SiO_4$, (2) natural fayalite, Fe_2SiO_4 (Smithsonian: R-3517-00: Rockport) and (3) silica (Alfa Aesar 99.995% purity). For laser coupling, silica was mixed with Fe metal powder (Aldrich 99.9%+ purity). Although San Carlos olivine contains enough Fe for laser coupling, to further improve the coupling, we mixed San Carlos olivine with Fe metal powder (20 wt%). Powders were ground and mixed in an alumina mortar, then cold-pressed into foils with a thickness of approximately 10 μm. Rhenium gaskets were indented by diamond anvils with 200 μm diameter culets and then drilled with 125 μm diameter holes. The rhenium gaskets were then coated with about 800 Å of gold to inhibit hydrogen diffusion into the gasket material. The gaskets were placed back onto the diamond culets, followed by the sample foils and spacers (of the same material as the sample foil), and gold and ruby grains for pressure calibration. The cells were then loaded with 1,300–1,500 bars of pure H_2 gas in a Sanchez GLS 1500 gas loading system and then compressed to the target pressures (measured using ruby fluorescence[45]) at 300 K before synchrotron laser-heating experiments. A fayalite sample was loaded with a 50:50 gas mixture of H_2 + Ar to examine the impact of a lower concentration of H_2.

Synchrotron experiments

In situ XRD images of the samples in the laser-heated diamond-anvil cell (LHDAC) were collected at the 13-IDD beamline of the GeoSoilEnviroConsortium for Advanced Radiation Sources sector at the Advanced Photon Source (APS) synchrotron facility. Near-infrared laser beams of wavelength 1,064 nm and monochromatic X-ray beams of wavelength 0.4133 Å or 0.3344 Å were coaxially aligned and focused on the sample in the LHDAC[46]. Standard continuous laser heating of H-loaded samples in the DAC results in an extremely mobile and diffusive hydrogen fluid that can penetrate diamond anvils, leading to diamond embrittlement and failure of the anvils[47]. To enable melting of silicates in a hydrogen medium, a pulsed laser-heating system was used to mitigate the amount of hydrogen diffusion into the anvils and the gasket material[29]. Each pulsed heating event consisted of 10^5 pulses at 10 kHz and 20 streak spectroradiometry measurements. The pulse width was 1 μs. Therefore, an event with 10^5 pulses gives a total heating time of 0.1 s. The X-ray spot size is 3×4 μm^2, and the laser-heating spot is a circle with a diameter of approximately 15 μm. The laser pulses were synchronized with the synchrotron X-ray detector such that diffraction measurements could take place only when the sample reached the highest temperature during heating. The small X-ray beam size and large laser-heating spot size help mitigate the effects of the radial thermal gradients in the high-temperature diffraction patterns. A previous study[46] showed that the laser-heating system provides a flat top laser beam intensity profile, which further reduces the radial thermal gradients in the hot spot. We also conducted two-dimensional XRD mapping after temperature quench of the samples in LHDAC at high pressures to monitor the possible effects of thermal gradients during laser heating. In the in situ high-temperature XRD patterns, it was difficult to distinguish broad diffuse scattering features from the melt because of the short duration of the measurements.

Although the heating duration is short, it was found that hydrogen is extremely reactive with molten silicates at high temperatures, overcoming the limited heating exposure time. Moreover, sample foils cold-compressed from powder permit hydrogen gas and fluid to percolate and surround individual grains (less than 1 μm in size). This creates a large surface area of the silicate exposed to hydrogen and, therefore, facilitates a fast reaction[48]. A recent study obtained consistent results between short pulse heating and continuous heating under hydrogen-rich conditions in diamond-anvil cells[49].

Thermal emission spectra from both sides of the sample in LHDAC were fitted to the grey-body equation to estimate the temperatures[46]. Temperatures are assigned from an average of temperatures recorded from 20 measurements (10 each upstream and downstream) over a heating event (Extended Data Table 1). Temperature uncertainty was calculated from the standard deviations (1σ) of these measurements. If the standard deviation is smaller than 100 K, from intrinsic uncertainties in the spectroradiometry method, we assigned 100 K for the uncertainty[50].

A Dectris Pilatus 1M CdTe detector was used to collect two-dimensional diffraction images. The diffraction images are integrated into one-dimensional diffraction patterns using the DIOPTAS package[51]. Diffraction patterns of CeO_2 and LaB_6 were measured for the correction of detector tilt and the determination of the sample-to-detector distance. Unit-cell parameter fitting was conducted by fitting the diffraction peaks with pseudo-Voigt profile functions in the PeakPo package[52]. Pressure was calculated from the unit-cell volume of a gold grain at the edge of the sample chamber using the equation of state of gold[53] before and after heating. A gold grain was placed away from the sample rather than mixing with it to prevent reactions or alloying with the sample material, and thus, pressure could not be measured at high temperatures during laser heating. A previous study[54] showed that the thermal pressure in a liquid Ar medium at temperatures of 1,000–4,000 K is 0.5–2.5 GPa in LHDAC. All of our experiments exceed the melting temperature of hydrogen. Therefore, thermal pressure should be similar to the above estimation in our experiments, and we assign a pressure uncertainty of 10% for high-temperature data points[23]. We note that this method does not introduce a severe error for this study, which is to explore the hydrogen–silicate reactions at high pressures.

Raman spectroscopy

Raman measurements were conducted using the Raman spectroscopy system at GeoSoilEnviroConsortium for Advanced Radiation Sources[55] for the identification of O–H and Si–H vibrations after heating. Raman scattering of the sample in a diamond-anvil cell was excited by a monochromatic 532-nm beam from a Coherent VERDI V2 laser. Raman spectra were collected over a wide range of wavenumbers (1,400–4,500 cm^{-1}) using a Princeton Instruments Acton Series SP-2560 spectrograph and PIXIS100 detector.

Modelling for the dynamics of the interior

The thermal evolution model is calculated for the entire interior (from centre to surface) on one mass grid, with no distinction between core and envelope (Fig. 3). The model is one-dimensional and solves the standard interior structure and evolution equations, which allow for heat transport by convection, radiation and conduction, depending on local conditions over time (equations can be found in ref. 56). The basic set of parameters for rocky planets with gas envelopes is adopted from ref. 28. The redistribution of composition by convective mixing, in which the convection criterion is fulfilled, is calculated as in ref. 56.

The input equations of state are from ref. 57 for hydrogen and helium, and an improved version of ref. 58 for water and silica as representatives of volatiles and refractories, respectively. In our experiments, we found that multiples of components, such as SiH_4 and MgH_2, apart from H_2O, can exist in H_2 envelopes. In this system, semi-convection (double diffusive convection) might develop under certain conditions (Supplementary Discussion 14), which could limit the mixing efficiency and terminate water production earlier than our models suggest. Irradiation by the parent star is included as a temperature boundary for a plane-parallel grey atmosphere with an optical depth of 1. The radiative opacity is that of a grain-free solar metallicity atmosphere[59].

Data availability

The experimental data that support the findings of this study are available from the corresponding authors upon reasonable request.

The XRD and Raman data are available at Zenodo (https://doi.org/10.5281/zenodo.15586691)[60]. An overview of the data is also included there. Source data are provided with this paper.

Code availability

Supplementary codes used in this study can be found at Zenodo[61] (https://doi.org/10.5281/zenodo.15678598).

45. Piermarini, G. J., Block, S., Barnett, J. D. & Forman, R. A. Calibration of the pressure dependence of the R_1 ruby fluorescence line to 195 kbar. *J. Appl. Phys.* **46**, 2774–2780 (1975).
46. Prakapenka, V. et al. Advanced flat top laser heating system for high pressure research at GSECARS: application to the melting behavior of germanium. *High Press. Res.* **28**, 225–235 (2008).
47. Deemyad, S. et al. Pulsed laser heating and temperature determination in a diamond anvil cell. *Rev. Sci. Instrum.* **76**, 125104 (2005).
48. Fu, S., Chariton, S., Prakapenka, V. B., Chizmeshya, A. & Shim, S.-H. Stable hexagonal ternary alloy phase in Fe-Si-H at 28.6–42.2 GPa and 3000 K. *Phys. Rev. B* **105**, 104111 (2022).
49. Fu, S., Chariton, S., Prakapenka, V. B. & Shim, S.-H. Core origin of seismic velocity anomalies at Earth's core–mantle boundary. *Nature* **615**, 646–651 (2023).
50. Kulka, B. L., Dolinschi, J. D., Leinenweber, K. D., Prakapenka, V. B. & Shim, S.-H. The bridgmanite–akimotoite–majorite triple point determined in large volume press and laser-heated diamond anvil cell. *Minerals* **10**, 67 (2020).
51. Prescher, C. & Prakapenka, V. B. DIOPTAS: a program for reduction of two-dimensional X-ray diffraction data and data exploration. *High Press. Res.* **35**, 223–230 (2015).
52. Shim, S.-H. PeakPo: a python software for x-ray diffraction analysis at high pressure and high temperature. *Zenodo* https://doi.org/10.5281/zenodo.3376238 (2019).
53. Ye, Y., Prakapenka, V., Meng, Y. & Shim, S.-H. Intercomparison of the gold, platinum, and MgO pressure scales up to 140 GPa and 2500 K. *J. Geophys. Res. Solid Earth* **122**, 3450–3464 (2017).
54. Dewaele, A., Fiquet, G. & Gillet, P. Temperature and pressure distribution in the laser-heated diamond–anvil cell. *Rev. Sci. Instrum.* **69**, 2421–2426 (1998).
55. Holtgrewe, N., Greenberg, E., Prescher, C., Prakapenka, V. B. & Goncharov, A. F. Advanced integrated optical spectroscopy system for diamond anvil cell studies at GSECARS. *High Press. Res.* **39**, 457–470 (2019).
56. Vazan, A., Helled, R., Kovetz, A. & Podolak, M. Convection and mixing in giant planet evolution. *Astrophys. J.* **803**, 32 (2015).
57. Saumon, D., Chabrier, G. & van Horn, H. M. An equation of state for low-mass stars and giant planets. *Astrophys. J. Suppl. Ser.* **99**, 713 (1995).
58. Vazan, A., Kovetz, A., Podolak, M. & Helled, R. The effect of composition on the evolution of giant and intermediate-mass planets. *Mon. Not. R. Astron. Soc.* **434**, 3283–3292 (2013).
59. Freedman, R. S. et al. Gaseous mean opacities for giant planet and ultracool dwarf atmospheres over a range of metallicities and temperatures. *Astrophys. J. Suppl. Ser.* **214**, 25 (2014).
60. Shim, S.-H. Experimental data for hydrogen-silicate reaction [Data set]. *Zenodo* https://doi.org/10.5281/zenodo.15586691 (2025).
61. Shim, S.-H. Jupyter notebooks for Supplementary Codes (0.0.1). *Zenodo* https://doi.org/10.5281/zenodo.15678598 (2025).
62. Sakamaki, K. et al. Melting phase relation of FeH_x up to 20 GPa: implication for the temperature of the Earth's core. *Phys. Earth Planet. Interiors* **174**, 192–201 (2009).
63. Mosenfelder, J. L., Asimow, P. D. & Ahrens, T. J. Thermodynamic properties of Mg2SiO4 liquid at ultra-high pressures from shock measurements to 200 GPa on forsterite and wadsleyite. *J. Geophys. Res. Solid Earth* **112**, B06208 (2007).
64. Ohtani, E. Melting relation of Fe_2SiO_4 up to about 200 kbar. *J. Phys. Earth* **27**, 189–208 (1979).
65. Andrault, D. et al. Melting behavior of SiO_2 up to 120 GPa. *Phys. Chem. Miner.* **47**, 10 (2020).
66. Zha, C., Liu, H., Tse, J. S. & Hemley, R. J. Melting and high *P–T* transitions of hydrogen up to 300 GPa. *Phys. Rev. Lett.* **119**, 075302 (2017).
67. Narygina, O. et al. X-ray diffraction and Mössbauer spectroscopy study of fcc iron hydride FeH at high pressures and implications for the composition of the Earth's core. *Earth Planet. Sci. Lett.* **307**, 409–414 (2011).
68. Thompson, E. et al. High-pressure geophysical properties of fcc phase FeH_x. *Geochem. Geophys. Geosyst.* **19**, 305–314 (2018).
69. Kato, C. et al. Stability of fcc phase FeH to 137 GPa. *Am. Mineral.* **105**, 917–921 (2020).
70. Tagawa, S., Gomi, H., Hirose, K. & Ohishi, Y. High-temperature equation of state of FeH: implications for hydrogen in Earth's inner core. *Geophys. Res. Lett.* **49**, e2021GL096260 (2022).
71. Ikuta, D. et al. Interstitial hydrogen atoms in face-centered cubic iron in the Earth's core. *Sci. Rep.* **9**, 7108 (2019).
72. Shibazaki, Y. et al. High-pressure and high-temperature phase diagram for $Fe_{0.9}Ni_{0.1}$–H alloy. *Phys. Earth Planet. Inter.* **228**, 192–201 (2014).
73. Ohta, K., Suehiro, S., Hirose, K. & Ohishi, Y. Electrical resistivity of fcc phase iron hydrides at high pressures and temperatures. *Comptes Rendus Geosci.* **351**, 147–153 (2019).
74. Dorogokupets, P. I., Dymshits, A. M., Litasov, K. D. & Sokolova, T. S. Thermodynamics and equations of state of iron to 350 GPa and 6000 K. *Sci. Rep.* **7**, 41863 (2017).
75. Piet, H. et al. Superstoichiometric alloying of H and close-packed Fe-Ni metal under high pressures: implications for hydrogen storage in planetary core. *Geophys. Res. Lett.* **50**, e2022GL101155 (2023).

Acknowledgements We thank Y. Fei and G. Huss for their comments and questions, which improved the quality of this paper. S.-H.S. and H.W.H. were supported by the National Science Foundation (NSF) grants AST-2108129, AST-2406790 and EAR-1921298. Portions of this work were performed at GeoSoilEnviroCARS (The University of Chicago, Sector 13), Advanced Photon Source, Argonne National Laboratory. GeoSoilEnviroCARS is supported by the NSF, Earth Sciences (EAR-1634415). This research used resources of the Advanced Photon Source, a US DOE Office of Science User Facility operated for the DOE Office of Science by the Argonne National Laboratory under contract no. DE-AC02-06CH11357. We acknowledge the use of facilities in the Eyring Materials Center at ASU. Part of this work was performed under the auspices of the US DOE by Lawrence Livermore National Laboratory under contract DE-AC52-07NA27344. The opinions are those of the authors and do not necessarily represent the opinions of LLNL, LLNS, DOE, NNSA or the US government. The US government, and the publisher, by accepting the article for publication, acknowledge that the US government retains a non-exclusive, paid-up, irrevocable, worldwide licence to publish or reproduce the published form of this manuscript, or allow others to do so, for US government purposes (release authorization no. LLNL-JRNL-872168). A.V. acknowledges support by ISF grants 770/21 and 773/21.

Author contributions H.W.H. and S.-H.S. conceived the project; H.W.H., S.C., V.B.P. and S.-H.S. conducted the synchrotron experiments; A.V. conducted sub-Neptune modelling; H.W.H. and S.-H.S. analysed the results; and H.W.H., S.-H.S. and A.V. wrote the paper. All authors reviewed the paper.

Competing interests The authors declare no competing interests.

Additional information
Supplementary information The online version contains supplementary material available at https://doi.org/10.1038/s41586-025-09630-7.

Correspondence and requests for materials should be addressed to H. W. Horn or S.-H. Shim.

Peer review information *Nature* thanks Yingwei Fei, Gary Huss and the other, anonymous, reviewer(s) for their contribution to the peer review of this work. Peer reviewer reports are available.

Reprints and permissions information is available at http://www.nature.com/reprints.

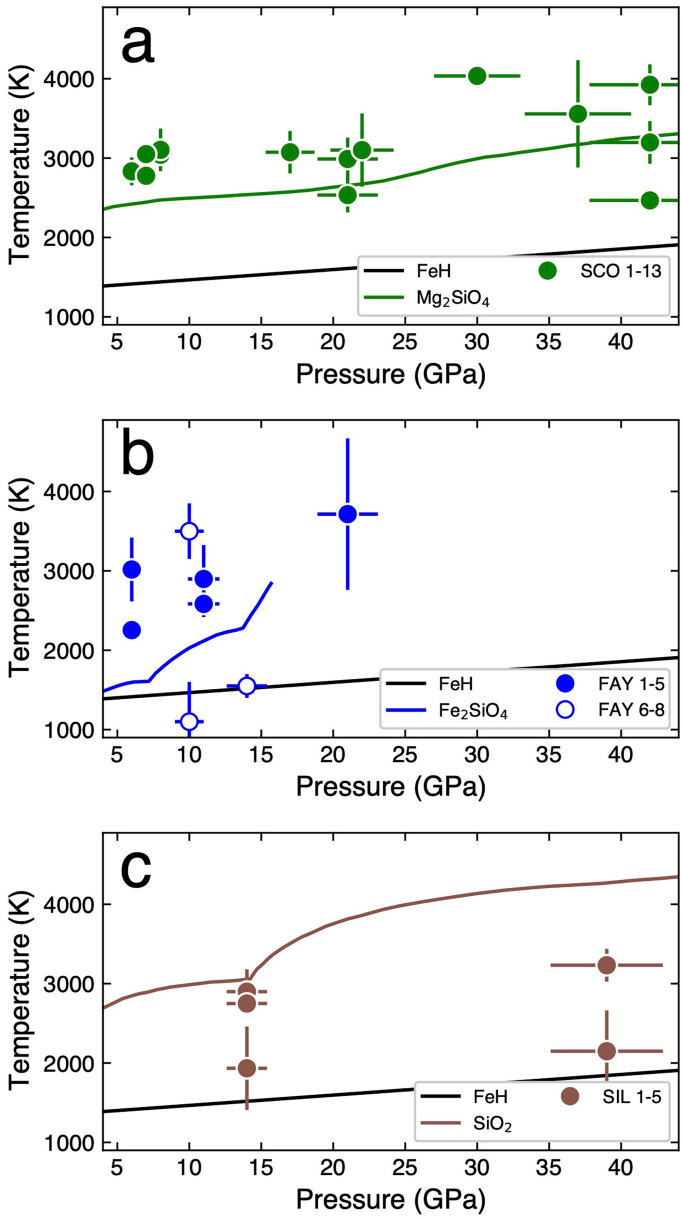

Extended Data Fig. 1 | Pressure-temperature conditions of the experimental runs. a, San Carlos olivine, **b**, fayalite, and **c**, silica starting materials in this study (Extended Data Table 1). For fayalite, three experimental runs were conducted with a 50% Ar + 50% H_2 medium (open circles). Melting curves for the relevant phases are shown: FeH_x (ref. 62); Mg_2SiO_4 (ref. 63); Fe_2SiO_4 (ref. 64); SiO_2 (ref. 65). All the experiments were conducted above the melting temperature of hydrogen[66]. While olivine and fayalite couple with laser beams sufficiently well for melting, lack of Fe in silica makes it difficult to heat above melting as shown in **c**.

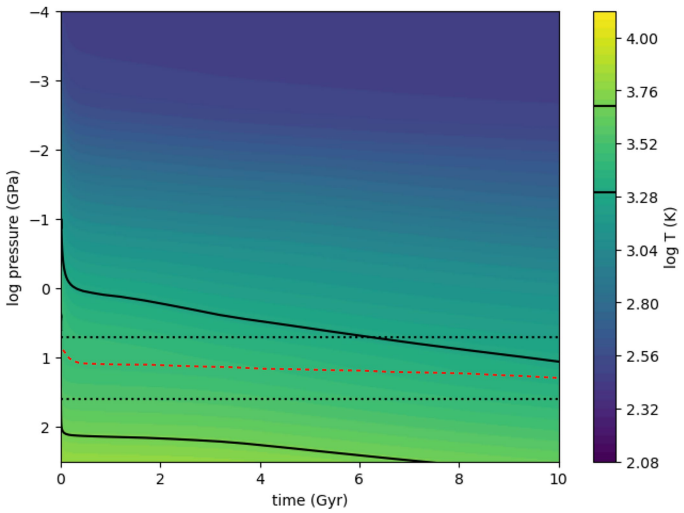

Extended Data Fig. 2 | Thermal evolution of a rocky 5 M_E sub-Neptune planet with an H + He (5 wt%) envelope. Shown is the temperature (color) as a function of pressure (*y*-axis) in the interior from the center up to 1 bar pressure, as a function of time (*x*-axis). The range of pressure (dotted black) and temperature (solid black) in which water production is expected according to the experiments is shown. The red dashed line signifies the mantle-envelope interface. Model is based on ref. 28.

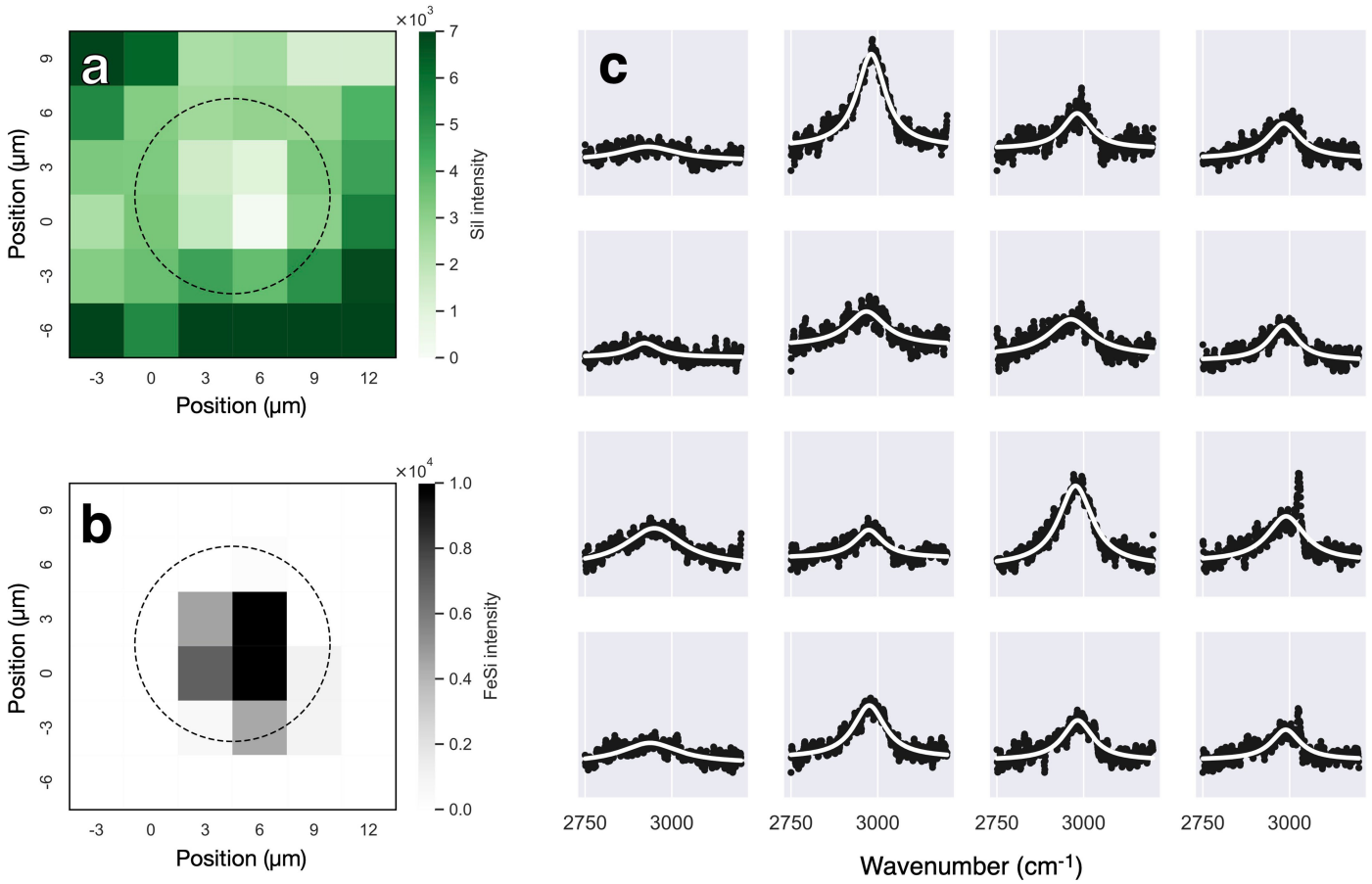

Extended Data Fig. 3 | Analysis of the samples after heating in a hydrogen medium in LHDAC. Two dimensional maps of the XRD intensities of **a**, silicates and **b**, B2 $Fe_{1-y}Si_y$ after heating the sample in SCO-11. The anti-correlation between the two at the heating spot center (dashed circle) shows that when melted silicates (bdm) break down, Si is reduced to form $Fe_{1-y}Si_y$. **c**, Raman-active OH vibration from H_2O ice after heating silica + Fe metal. The Raman spectra were measured for a 20 × 20 μm^2 heated area. The distance between the spots where the spectra were collected is 5 μm. The spectra were collected after laser heating at 14 GPa.

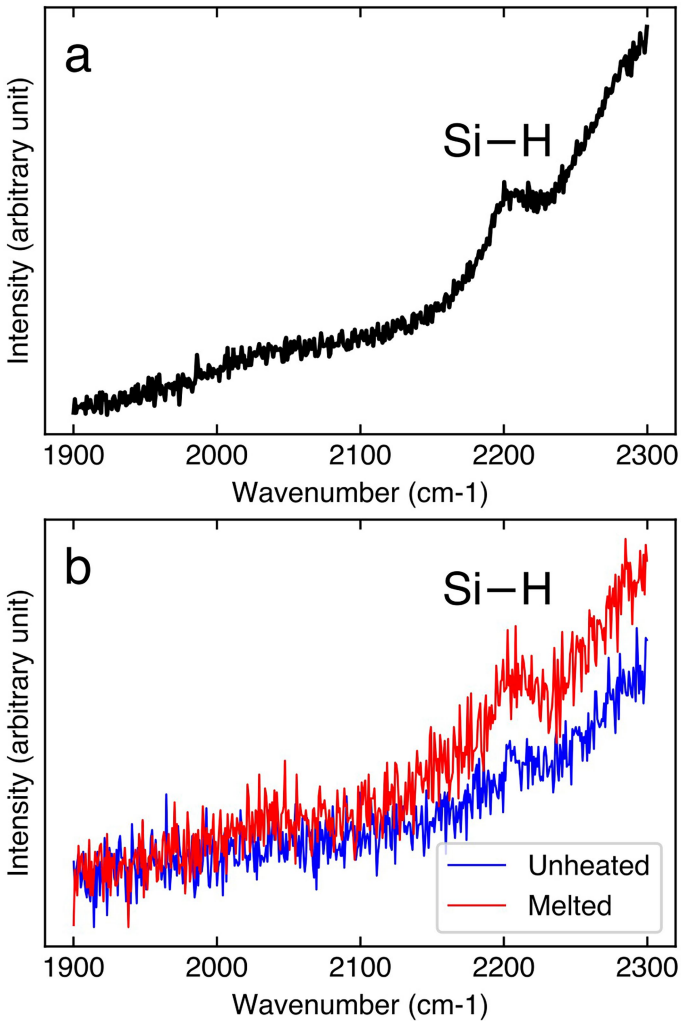

Extended Data Fig. 4 | Raman spectra from run FAY-8 where starting fayalite was heated to 1550 K at 14 GPa. The measurements were conducted after temperature quench to 300 K and decompression to 2.5 GPa. The Si–H vibrational mode was detected at the melted area (**a**). No such feature was observed outside the melted area (blue, **b**). In **b**, we also include spectrum measured at the melted spot (red) for the same exposure time. The same mode has been documented for silica melted in hydrogen at 2–3 GPa (ref. 26).

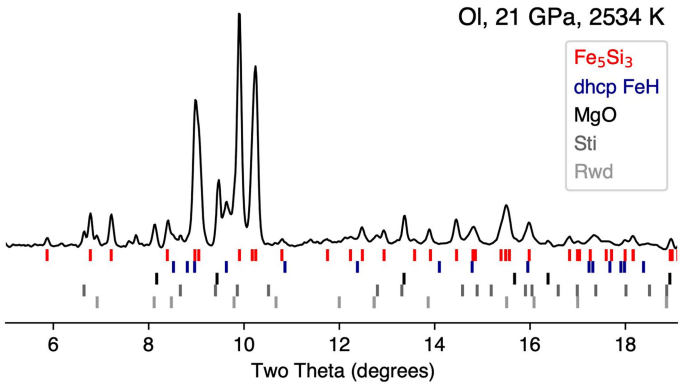

Extended Data Fig. 5 | X-ray diffraction pattern measured after heating a starting mixture of San Carlos olivine and Fe metal to 2534 K at 21 GPa (run SCO-7). The ticks below the diffraction pattern are the peak positions of the observed phases. The names of the phases in the legend is ordered same as the ticks from top to bottom. X-ray energy is 37 keV.

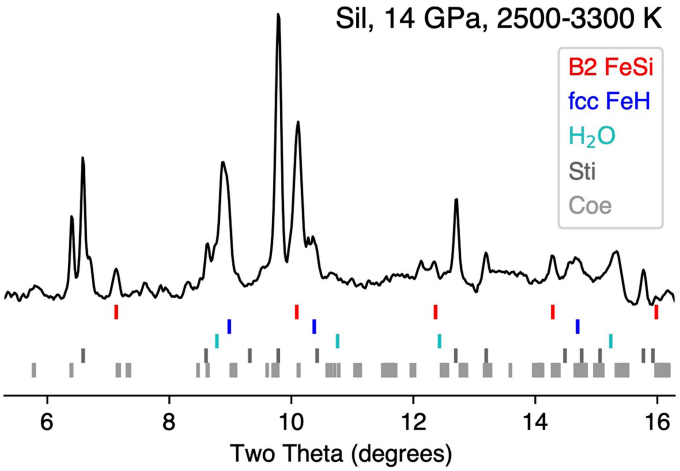

Extended Data Fig. 6 | X-ray diffraction pattern measured after heating a silica starting material in a hydrogen medium to 2899 K (below the melting temperature) at 14 GPa (run SIL-2). The ticks below the diffraction pattern are the peak positions of the observed phases. The names of the phases in the legend is ordered same as the ticks from top to bottom. X-ray energy is 37 keV.

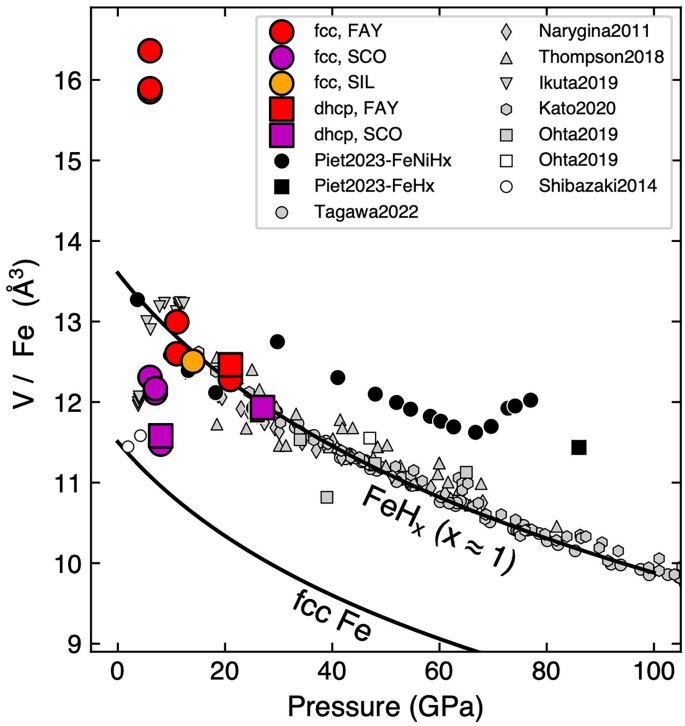

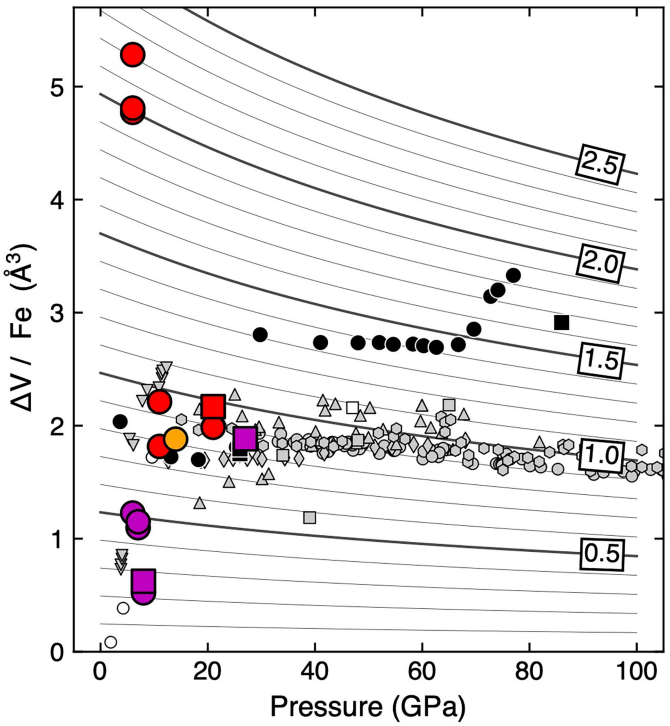

Extended Data Fig. 7 | Atomic volume (left) and volume increase by H incorporation, *V* (right), of FeH_x observed in different runs (colored symbols). The volumes were measured after heating at 300 K. For comparison, the figures also include data points from previous studies[67–73]. The equations of state for fcc Fe (H/Fe = 0) and fcc FeH (H/Fe = 1) are from ref. 74 and ref. 69, respectively. The data points measured for the solid phases quenched from (Fe,Ni)-H liquid are shown as black symbols[75]. The concentration curves (*x*) shown in the right figure are from the density functional theory calculation in ref. 75.

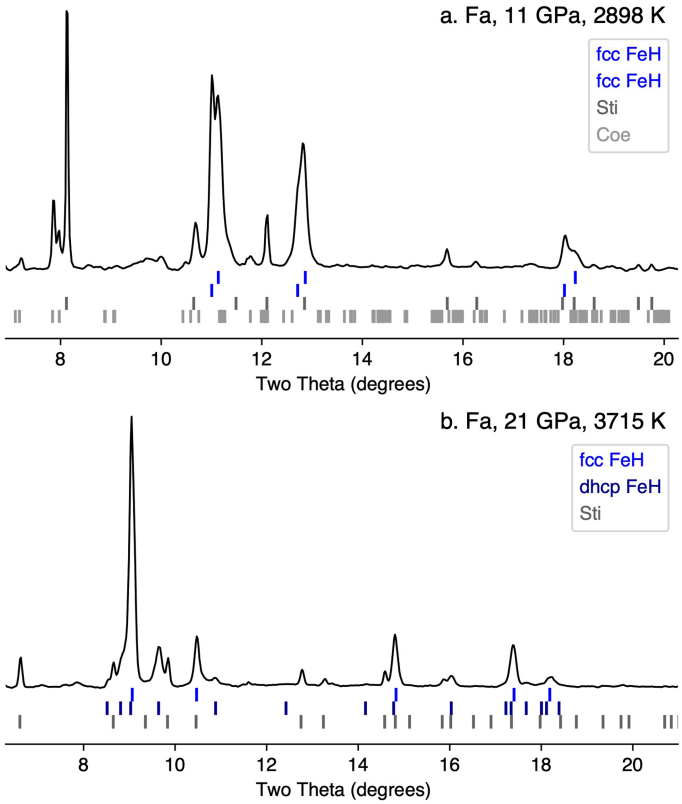

Extended Data Fig. 8 | X-ray diffraction pattern measured after heating a fayalite starting material in a hydrogen medium to a, 2898 K at 11 GPa (run FAY-3) and b, 3715 K at 21 GPa (run FAY-5). a was measured at 6 μm away from the heating center. Two separate fcc phases with different volumes (and therefore different levels of hydrogenation) are observed, likely because of different rate of temperature decrease during quenching at different spots and loss of hydrogen during quench of FeH_x melt[75]. The ticks below the diffraction patterns are the peak positions of the observed phases. The names of the phases in the legend is ordered same as the ticks from top to bottom. X-ray energy is **a**, 30 keV and **b**, 37 keV.

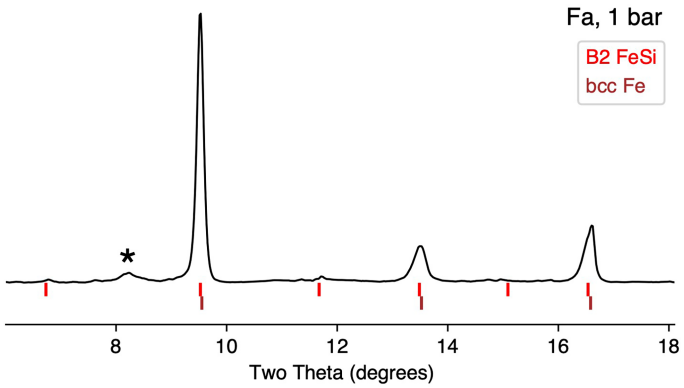

Extended Data Fig. 9 | X-ray diffraction pattern measured after the decompression of a fayalite starting material heated in a hydrogen medium to 3017 K at 6 GPa (run FAY-1). The diffraction pattern was measured at 1 bar and 300 K. The ticks below the diffraction pattern are the peak positions of the observed phases. The names of the phases in the legend is ordered same as the ticks from top to bottom. "*" indicates a feature from detector defects. X-ray energy is 37 keV.

Extended Data Table 1 | Experimental runs in this study

Run	P (GPa)	T (K)	A.M.	Result
		$(Mg_{0.9}Fe_{0.1})_2SiO_4$ + Fe + H		
SCO-1	8	3042(159)	XRD, SEM	$Fe_{1-y}Si_y$, MgO
SCO-2	6	2833(177)	XRD, SEM	FeH_x, MgO
SCO-3	8	3104(269)	XRD, SEM	$Fe_{1-y}Si_y$, FeH_x, MgO
SCO-4	7	3050(100)	XRD, SEM	$Fe_{1-y}Si_y$, FeH_x, MgO
SCO-5	7	2777(100)	XRD, SEM	$Fe_{1-y}Si_y$, FeH_x, MgO
SCO-6	17	3074(267)	XRD	Fe_5Si_3, $Fe_{1-y}Si_y$, FeH_x, MgO, Rwd, Wds
SCO-7	21	2534(218)	XRD	Fe_5Si_3, FeH_x, Sti, MgO, Rwd
SCO-8	21	2738(119), 2989(269)	XRD	Fe_5Si_3, FeH_x, Sti, MgO
SCO-9	22	3101(462)	XRD	Fe_5Si_3, $Fe_{1-y}Si_y$, FeH_x, Sti, MgO, Rwd
SCO-10	30	3298(150), 2434(100), 2264(100), 2187(100), 2310(100), 2539(100), 4035(144)	XRD, SEM	$Fe_{1-y}Si_y$, FeH_x, MgO, Bdm
SCO-11	37	3557(677)	XRD	$Fe_{1-y}Si_y$, FeH_x, MgO, Bdm
SCO-12	42	2704(150), 2467(150)	XRD, SEM	FeH_x, Bdm, MgO
SCO-13a	42	2792(162), 2725(133), 3075(150), 3197(269)	XRD, SEM	FeH_x, Bdm, MgO
SCO-13b	42	3789(378), 3352(174), 3924(258)	XRD, SEM	$Fe_{1-y}Si_y$, FeH_x, MgO
		Fe_2SiO_4 + H		
FAY-1	6	3017(402)	XRD, Raman, SEM	$Fe_{1-y}Si_y$, FeH_x, Fe
FAY-2	6	2254(100)	XRD, Raman	$Fe_{1-y}Si_y$, FeH_x, Fe
FAY-3	11	2898(427)	XRD, Raman, SEM	FeH_x, Sti, Coe
FAY-4	11	2808(475), 2584(166)	XRD, Raman	FeH_x, Sti, Coe
FAY-5	21	3965(407), 3715(954)	XRD, Raman	FeH_x, Sti
		Fe_2SiO_4 + H + Ar (50% H_2)		
FAY-6	10	3500(350)	XRD, Raman	FeH_x, Sti, Coe
FAY-7	10	1100(500)	XRD, Raman	FeH_x, Sti, Coe
FAY-8	14	1550(150)	XRD, Raman	FeH_x, Sti, Coe
		SiO_2 + Fe + H		
SIL-1	14	1934(526)	XRD, Raman	$Fe_{1-y}Si_y$, FeH_x, Sti, Coe
SIL-2	14	2899(282)	XRD, Raman	$Fe_{1-y}Si_y$, Sti, Coe
SIL-3	14	2750(100)	XRD, Raman	$Fe_{1-y}Si_y$, FeH_x, Sti
SIL-4	39	2149(514)	XRD	$Fe_{1-y}Si_y$, Sti
SIL-5	39	1647(258), 2906(254), 3039(284), 3009(100), 3103(100), 3232(206)	XRD	$Fe_{1-y}Si_y$, Sti

Estimated uncertainties for pressure (P) are 10% (see the Methods section). In some runs, multiples of heating events (10^5 laser pulses at 10 kHz) were performed and therefore temperature for each individual heating events are provided. $Fe_{1-y}Si_y$ was observed in the B2 structure throughout these runs. FeH_x appears in the face-centered cubic (fcc) structure during heating and temperature-quenching. When Fe metal was loaded as a starting material (SCO and SIL runs), double hexagonal close packed (dhcp) structured FeH_x was also observed. Fe metal (Fe) was observed as body-centered cubic (bcc) at pressures lower than 10 GPa in some FAY runs. A.M.: analytical methods; XRD: X-ray diffraction; SEM: scanning electron microscopy; Raman: Raman spectroscopy; Rwd: ringwoodite; Wds: wadsleyite; Bdm: bridgmanite; Sti: stishovite; Coe: coesite.